# Highly selective PtCo bimetallic nanoparticles on silica for continuous production of hydrogen from aqueous phase reforming of xylose

*Minkyeong Kim [a,1], Arash Badakhsh [a,b,1], Shedrack G. Akpe [c],*
*Yoondo Kim [a,d], Ki-Jung Nam [a,e], Yongmin Kim [a], Hyangsoo Jeong [a,e],*
*Suk Woo Nam [a], Hyung Chul Ham [c,**], Sun Hee Choi [a,e,***],*
*Hyuntae Sohn [a,e,\*]*

[a] *Center for Hydrogen and Fuel Cell Research, Clean Technology Research Division, Korea Institute of Science and Technology (KIST), Seoul, 02792, Republic of Korea*
[b] *PNDC, University of Strathclyde, Glasgow, G68 0EF, United Kingdom*
[c] *Department of Chemistry and Chemical Engineering, Education and Research Center for Smart Energy Materials and Process, Inha University, Incheon, 22212, Republic of Korea*
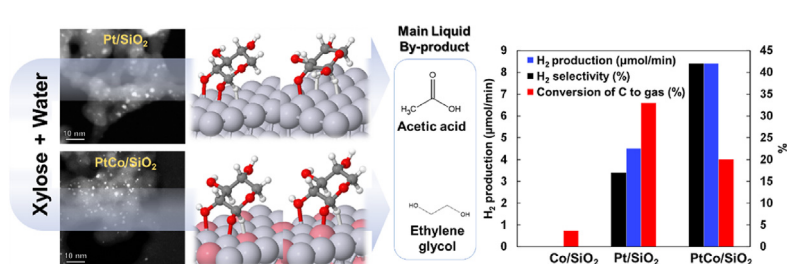[d] *Department of Chemical and Biological Engineering, Korea University, Seoul 02841, Republic of Korea*
[e] *Energy and Environment Technology, KIST School, University of Science & Technology (UST), Seoul, 02792, Republic of Korea*

## HIGHLIGHTS

- Silica (SiO$_2$)-supported PtCo bimetallic nano-catalyst was tested for APR of xylose.
- PtCo/SiO$_2$ demonstrated higher H$_2$ selectivity than monometallic Pt/SiO$_2$ and Co/SiO$_2$.
- Co/SiO$_2$ showed no catalytic activity for the APR of xylose.
- PtCo catalyst produced ethylene glycol, resulting in a higher H$_2$ production rate.
- DFT calculations confirmed that the surface layer of Co atoms enhances the activity.

## GRAPHICAL ABSTRACT

ABSTRACT

Hydrogen ($H_2$) is a promising energy vector for mitigating greenhouse gas emissions. Lignocellulosic biomass waste has been introduced as one of the abundant and carbon-neutral $H_2$ sources. Among those, xylose with its short carbon chain has emerged attractive, where $H_2$ can be catalytically released in an aqueous reactor. In this study, a composite catalyst system consisting of silica ($SiO_2$)-supported platinum (Pt)-cobalt (Co) bimetallic nanoparticles was developed for aqueous phase reforming of xylose conducted at 225 °C and 29.3 bar. The $PtCo/SiO_2$ catalyst showed a significantly higher $H_2$ production rate and selectivity than that of $Pt/SiO_2$, whereas $Co/SiO_2$ shows no activity in $H_2$ production. The highest selectivity for useful liquid byproducts was obtained with $PtCo/SiO_2$. Moreover, $CO_2$ emissions throughout the reaction were reduced compared to those of monometallic $Pt/SiO_2$. The PtCo bimetallic nanocatalyst offers an inexpensive, sustainable, and durable solution with high chemical selectivity for scalable reforming of hard-to-ferment pentose sugars.

## Introduction

The utilization of bioenergy has significantly increased in the past decades, and global warming by greenhouse gases has become a serious environmental issue worldwide [1]. Lignocellulosic biomass, mainly obtained from wood, corn stover, wheat straw, etc., has been extensively studied as an energy source to produce heat, electricity, and chemicals owing to its abundance in nature and carbon-neutral characteristics [2]. In recent years, hydrogen ($H_2$) production processes have received increased interest in the biomass conversion field because $H_2$ produced from biomass can generate renewable electricity in conjunction with a fuel cell [3]. There are various methods to extract $H_2$ from lignocellulosic biomass, such as implementing pyrolysis (>400 °C) [4], gasification (>750 °C) [5], steam reforming (>700 °C) [6], enzymatic decomposition processes (30−70 °C) [7]. However, the quantity of produced $H_2$ by these methods is low, and the reaction normally operates at high temperatures, lowering the overall energy efficiency [3,8].

Aqueous phase reforming (APR) is an alternative method for producing $H_2$ in a higher yield than other methods [9]. The process is operated at low temperature (200−250 °C) and high pressure (15−50 bar); hence, the reaction conditions are in liquid phase. The APR energy efficiency (~81% [10]) is higher than that of the normal steam reforming process (~60% [11]) because there is no need to evaporate the water and oxygenated hydrocarbons produced during the reaction. Moreover, an additional water-gas shift (WGS) reactor is not essential because the reaction occurs in a favorable temperature range for WGS, leading to low carbon monoxide formation and increased $H_2$ production rate in a single-step APR [12].

Many reactants related to the three polymeric components (cellulose, hemicellulose, and lignin) of lignocellulosic biomass have been tested for APR [9]. Sugar compounds such as glucose and xylose produced from the depolymerization of hemicellulose have been highlighted as reactants for APR because of their shorter carbon chain length than that of other products [13]. In particular, xylose, a C5 sugar-based chemical, is mostly wasted in conventional cellulosic ethanol production from lignocellulosic biomass because of the difficulties in fermenting xylose in the presence of glucose [14,15]. This is attributed to the carbon catabolite repression where microorganisms preferentially consume glucose over xylose through fermentation [16]. Consequently, scientific research on glucose has been more extensive than that on xylose with implications for applications in biohydrogen production, which was further extended to APR. On the other hand, the majority of research on xylose has focused on its fermentation process for the production of valuable chemicals, rather than hydrogen. For these reasons, recent studies have been more focused on $H_2$ production from the APR of xylose as an economically attractive way to produce $H_2$ from biomass-derived chemicals [17−19].

For the APR of sugars, the amount of hydrogen produced throughout the reaction depends on the mechanism favored over the catalyst. For example, it has been reported that the primary mechanism for $H_2$ formation is through C−C bond cleavage of the reactant and the subsequent WGS reaction [20,21]. When C−O bond cleavage becomes more favorable than C−C bond cleavage, side reactions occur, resulting in products such as alcohols and carboxylic acids [22]. Methanation is another competing mechanism in the APR reaction that produces methane from carbon dioxide, thereby lowering the overall $H_2$ selectivity [23]. Therefore, a catalyst with high selectivity towards C−C bond cleavage must be utilized to avoid side reactions and maximize $H_2$ yield. With respect to the catalyst, Pt metal has been extensively employed for the APR of sugars because it offers high activity and moderate selectivity [24,25]. For instance, Liu and Greeley [26] conducted a density functional theory (DFT) study on several catalysts (*i.e.*, Pt, Pd, Rh, and Cu) for glycerol dehydrogenation and concluded that both Pt and Pd exhibited high selectivity for C−C bond cleavage, but Pt exhibited a higher predicted activity. The experimental results obtained by R.R. Davda et al. [27] also suggested that, among silica-supported Pt, Ni, Ru, Rh, Pd, and Ir catalysts, Pt shows the highest activity in ethylene glycol APR, with an $H_2$ turnover frequency (TOF) of 5.5 times higher than that of Pd. In another study on the APR of sorbitol

to hexane, the authors suggested that the addition of Pt loading resulted in a higher rate of C−C cleavage [28].

The sintering of metallic nanoparticles at high temperatures is a well-known catalyst deactivation mechanism in thermochemical reactions. Additionally, when carbon-based feedstocks are involved in the reaction, they can lead to the formation of carbon deposits on the catalyst (i.e., coking), which reduces reactivity by blanketing active sites and/or disrupting electronic interactions between the catalyst and support. In the case of APR, several catalyst deactivation mechanisms have been identified, including coking, carbonate formation, sintering, re-oxidation, and leaching [24]. Reactions with water can also cause deactivation by leading to (re-)oxidation and/or leaching, which causes a loss of active species transferred to the liquid reactant [29,30]. Moreover, the formation of boehmite on alumina-supported catalysts during APR reaction can increase support surface acidity [31], leading to a preference for C−O cleavage. In summary, APR is subject to deactivation mechanisms that are typical in thermochemical reactions, as well as others that are associated with the presence of water as a reactant.

Incorporating a second element in metallic catalysts has been shown to improve the thermal stability (by increasing the support-catalyst interaction and delaying sintering) and resistance to coke formation and catalyst poisoning in heterogeneous catalysts [32]. Therefore, studies have been conducted to investigate the effect of promoters on the performance of Pt-based catalysts for the APR [24]. Among the common transition metal promoters, non-noble metals such as Co and Ni have been assessed for APR. For instance, Dosso et al. [33] compared the performance of bimetallic formulations supported on alumina ($Al_2O_3$) in the APR of polyols, showing that both PtNi and PtCo are more active than monometallic Pt catalysts, whereas Co addition mainly lowers coke formation and methane selectivity. Moreover, the catalytic performance of carbon-nanotube-supported Pt catalysts promoted with Co or Mo was investigated by Dietrich et al. [34] in glycerol APR. The addition of Co can effectively improve the coke resistance of catalysts [35]. In addition to the catalyst particle itself, the support material can dramatically affect catalytic performance. Due to its thermochemical stability and high metal-support interaction, $Al_2O_3$ has been extensively investigated as a promising support interaction. However, the transition from $Al_2O_3$ to boehmite (AlO(OH)) has been reported as one of the main challenges in APR applications [36,37].

In this study, to develop a practical route for sustainable $H_2$ production, we conducted a continuous APR of xylose over PtCo bimetllic nanoparticles supported on $SiO_2$ and compared its activity with that of $SiO_2$-supported monometallic Pt or Co catalysts. We selected non-reducible $SiO_2$ (50.4 USD/t − industrial sand basis [38]) as the catalyst support because it is a more cost-effective than $Al_2O_3$ (500 USD/t [38]) and has a significantly higher surface area. Various reaction conditions were evaluated to identify and optimize the correlation between the catalyst activity and APR process. All the catalysts were characterized by X-ray powder diffractometry (XRD), transmission electron microscopy (TEM), $N_2$-sorption, temperature-programmed reduction (TPR), X-ray photoelectron spectroscopy (XPS), extended X-ray absorption fine structure (EXAFS) to investigate the chemical and physical properties of the catalyst as well as to investigate the formation of PtCo nanoalloys. Finally, DFT calculations were conducted to determine the adsorption and reaction energies of the first dehydrogenation of xylose on the PtCo surface to understand the enhanced activity when Co was added.

## Experimental

### Materials

Chloroplatinic acid ($H_2PtCl_6 \cdot xH_2O$, Sigma-Aldrich) and cobalt nitrate hexahydrate ($Co(NO_3)_2 \cdot 6H_2O$, Sigma-Aldrich) were used as the metal precursors for the synthesis of $Pt/SiO_2$ and $Co/SiO_2$, respectively. Fumed silica ($SiO_2$; Sigma-Aldrich) was used as the catalyst support.

### Catalyst synthesis

Monometallic Pt- or Co-based samples were synthesized by the wet impregnation (incipient wetness) method. The metal precursor powders were first dissolved in deionized water, where the pH of the precursor solution was maintained at 1 using 0.1 M of HCl solution. 2.5 g of $SiO_2$ was added to the solution to obtain 5 wt % $Pt/SiO_2$ and $Co/SiO_2$ for each sample. The resulting suspension was homogeneously mixed at 70 °C for 3 h prior to drying in a rotary evaporator at 130 °C. The product sample was fully dried at 110 °C in a convection oven overnight. The final dried catalyst was calcined at 400 °C in the air for 5 h to transform the metal precursors into their oxide form. For $PtCo/SiO_2$, 2.5 wt % of Pt and Co were loaded to the sample under identical synthesis conditions as mentioned above. Prior to catalyst characterization, all samples were pre-reduced ex situ for 2 h at 500 °C using 10% $H_2/Ar$, except for the TPR experiment.

### Catalyst characterization

#### Inductively coupled plasma atomic emission spectroscopy (ICP-AES)
The actual Pt and Co metal contents in the samples were measured by ICP-AES using a Horiba Jobin Yvon Ultima, Horiba France Sas. Prior to measurements, all samples were pre-reduced and dissolved in $HF/HNO_3/HCl$ solutions.

#### Brunauer−Emmett−Teller (BET) surface area and pore volume
The $N_2$ physisorption technique was employed using a Micromeritics accelerated surface area and porosimetry instrument (ASAP 2000, Micromeritics) to obtain the Brunauer-Emmett-Teller (BET) surface area and pore volume of the catalysts. The pre-reduced sample was first degassed at 250 °C under vacuum for catalyst surface cleaning purposes before the experiment. $N_2$ molecules were then adsorbed on the sample surface at the liquid nitrogen temperature by varying the relative pressure ($P/P_o$). The pore size distribution curve was acquired using the Barrett-Joyner-Halenda (BJH) model.

#### X-ray diffractometry (XRD)
Structural analysis of the pre-reduced samples was conducted using an X-ray diffractometer (XRD, D8 Advanced, Bruker)

with CuK$\alpha$ radiation ($\lambda$ = 0.15418 nm) at 40 kV and 40 mA. The diffraction pattern was recorded from $2\theta$ = $10°$–$90°$ at a scan rate of 2 °/min, and the measured peaks were identified by the JCPDS (Joint Committee on Powder Diffraction Standards) references.

### X-ray photoelectron spectroscopy (XPS)

The XPS spectra of the pre-reduced samples were acquired by K-Alpha+ XPS (ThermoFisher Scientific) using a monochromatic Al K$\alpha$ anode (spot sizes of 1486.6, 12 kV, 1.16 mA, and 400 $\mu$m). The pressure during measurement was less than $2 \times 10^{-7}$ mbar.

### Temperature-programmed reduction (TPR)

Temperature-programmed reduction (H$_2$-TPR) was performed using BelcatII (Microtrac) equipped with a thermal conductivity detector (TCD) to reveal the reduction behavior of the samples. 25–50 mg of sample powder was loaded in a quartz tube insulated by glass fiber and was thermally treated at 500 °C for 2 h in pure Ar. The sample bed temperature was then naturally cooled down to 50 °C. After stabilizing the TCD signal for 30 min at 50 °C, the temperature was slowly increased to 900 °C at a ramp rate of 5 °C/min using 10% H$_2$/Ar.

### Transmission electron microscope (TEM) and high angle annular dark-field scanning transmission electron microscopy (HAADF-STEM) imaging

TEM and HAADF-STEM (Talos, FEI, ThermoFisher Scientific) images were collected over the *ex situ* reduced Pt and Co catalysts. The samples were prepared by dispersing the powder in ethanol and loading the suspension onto a carbon-film TEM grid (CF200–Cu, Electron Microscopy Sciences). The particle size distribution of the samples was determined using the ImageJ software.

### X-ray absorption spectroscopy (XAS)

The formation of the PtCo nanoalloys was investigated using XAS. The extended X-ray absorption fine structure (EXAFS) spectra of the pre-reduced PtCo/SiO$_2$ catalyst were acquired at the PLS-II 10C wide XAFS beamline, Pohang Accelerator Laboratory (PAL), located in Pohang City, Republic of Korea. The Pt L3-edge (11563.7 eV) was recorded in both the transmittance and fluorescence modes using Si(111) and Si(311) double crystal monochromators. Platinum (II) chloride and platinum foil were used as standards and their spectra were collected. First, the samples were finely ground, pressed into pellets, and then moved to the center of the beam. The oxidation state of the PtCo/SiO$_2$ catalyst was calculated using a linear combination of the spectra of the two standards in the Athena software. The bond distances to the neighboring atoms and the coordination number of Pt were estimated by conducting quantitative EXAFS fitting in Artemis software, where the single-scattering paths were calculated for Pt–Pt, Pt–O, and Pt–Co using Feff calculations.

### Catalytic activity testing: APR of xylose

APR of 3 wt% xylose aqueous solution was conducted in a fixed-bed continuous reactor. The xylose APR reaction is shown in Eq. (1). First, the xylose powder was dissolved in deionized water and magnetically stirred for 30 min at room temperature. The reactor with a length of 8 cm and 0.95 cm of diameter was filled with 300 mg of catalyst, which was then reduced *in situ* at 500 °C in 10% H$_2$/Ar for 2 h. After the reactor was cooled down to 195–235 °C depending on the experimental conditions, the reactor pressure was raised to 29.3 bar using pure N$_2$ gas (30 ml/min) controlled by a thermal mass flow controller (MFC, Bronkhorst) and a back pressure regulator (BPR, Bronkhorst). The reactor pressure was continuously monitored using an electrical pressure gauge. 3 wt % xylose feed was injected using a high-performance liquid chromatography pump (HPLC pump; Series 1500, LabAlliance) at a range of space velocities of 2–32 g/g$_{Cat}$/h depending on the reaction conditions. The reactor outlet was connected to a vapor–liquid separator. The separated gas products were analyzed using a gas chromatograph (GC, 9780 A, Agilent) equipped with a double column (HP-MOLESIEVE capillary, HP-PLOT/Q capillary) and a thermal conductivity detector (TCD). The total flow rate of the product stream was estimated using an internal standard of N$_2$. At the end of the experiment, the effluent liquid was drained from the separator and analyzed using high-performance liquid chromatography (HPLC, YL 9100, Young In Chromass) equipped with an HPX-87H column and a refractive index detector (RID). The conversion of carbon (C) to gas, H$_2$ selectivity, and liquid product selectivity for the APR reaction were calculated using Eq. (2) to Eq. (4) (RR refers to the theoretical H$_2$/CO$_2$ reforming ratio for xylose, APR = 2):

$$C_5H_{10}O_5 + 5H_2O \rightarrow 10H_2 + 5CO_2 \tag{1}$$
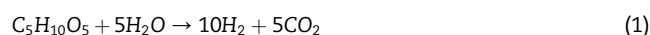
$$\text{Conversion of C to gas (\%)} = 100 \times \frac{mol_{out,carbon}}{mol_{in,xylose} \times 5} \tag{2}$$

$$\text{Selectivity to H}_2 \text{ (\%)} = 100 \times \frac{mol_{out,H2}}{mol_{out,carbon}} \times \frac{1}{RR} \tag{3}$$

$$\text{Liquid product selectivity (\%)} = 100 \\ \times \frac{\text{mol of liquid products}}{\text{mol of total liquid products}} \tag{4}$$

$$\text{H}_2 \text{ production rate} = \frac{mol_{out,H2}}{mol_{out,gas}} \times \text{Total flow rate}$$

### Density functional theory (DFT) calculation

DFT calculations were conducted to clarify the improved activity of the PtCo/SiO$_2$ catalyst in the APR of xylose. Plane-wave spin-polarized calculations were performed using the Vienna ab initio simulation package (VASP) [39], which solves self-consistent algorithms using the Kohn-Sham equations. A plane-wave basis set with a kinetic energy cutoff of 400 eV was used to describe the valence electrons, while the electron-ion core interactions were described using projected augmented wave (PAW) [39] pseudopotentials1 within the Perdew-Burke-Eenzerhof (PBE) [40] exchange-correlation functional. For both the adsorption studies and reactions occurring on different surfaces, the irreducible Brillouin-zone integrations were sampled with a $1 \times 1 \times 1$ Monkhorst–Pack k-point mesh. A $6 \times 4$ supercell containing three layers [41] with bottom layer fixed and top two layers, including the adsorbate relaxed, was

used as our model catalyst Convergence criteria of $1 \times 10^{-6}$ eV and 0.05 eV/Å were chosen for the ionic and electronic relaxations of slabs and adsorbates, respectively.

## Results and discussion
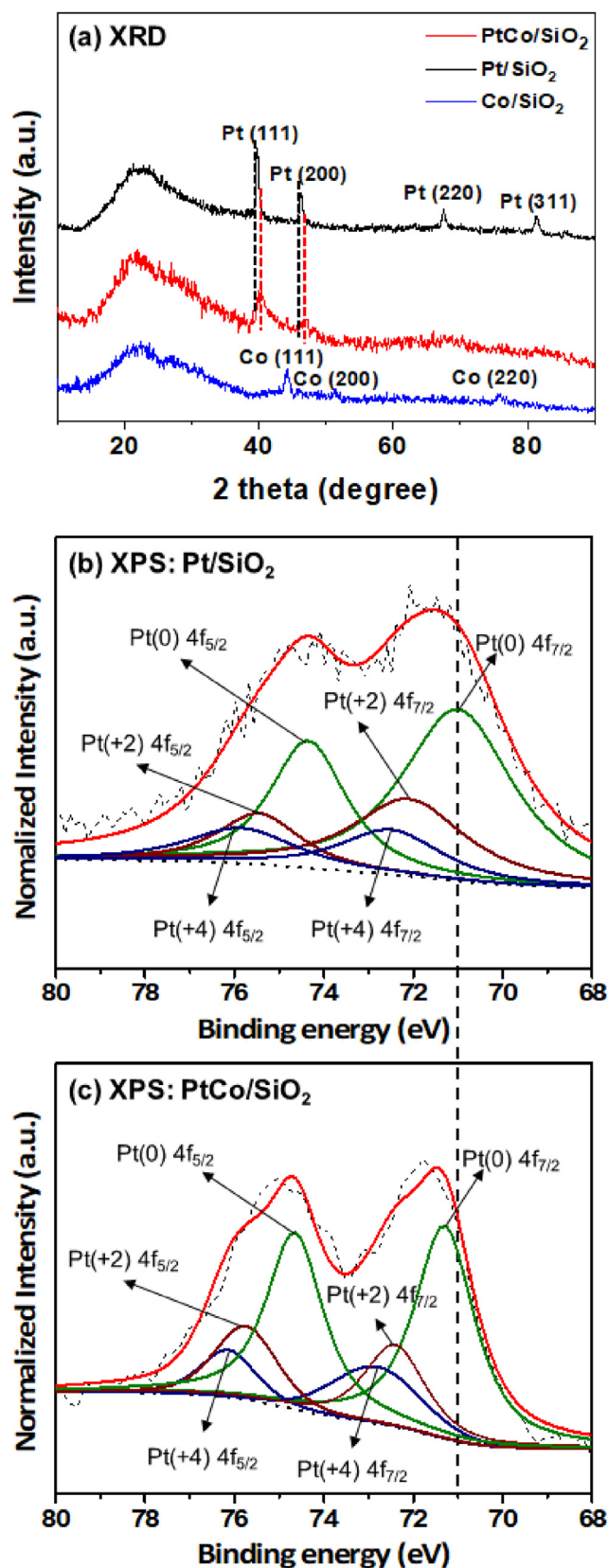
### Metal loading, BET surface area and pore volume

The physical and chemical characteristics of the *ex situ* reduced catalysts (at 500 °C for 2 h in 10% $H_2$/Ar) are summarized in Table 1. Compared with the monometallic Pt/SiO₂ catalyst, a 2.36 times reduction in the loading of costly Pt was observed for the PtCo/SiO₂ catalyst. This was achieved while maintaining the surface area and total pore volume of the monometallic Pt/SiO₂, as these values are approximately the same for the bimetallic PtCo/SiO₂ catalyst. On the other hand, the surface area and total pore volume showed the highest reduction for Co/SiO₂ compared to pristine SiO₂. The higher decrease in surface area and pore volume after Co impregnation of the SiO₂ support was possibly attributed to the agglomeration of Co particles on the catalyst surface, as evidenced by the TEM images. Each of the metal loaded catalysts exhibits a significant increase in total pore volume compared to the bare SiO₂ support. This increase is mainly attributed to the HCl treatment used during catalyst synthesis, in which a 0.1 M HCl solution was utilized to dissolve the metal precursor powders, resulting in an acidic solution with a pH of 1. The HCl treatment leads to a highly disordered and porous SiO₂ support with an enhanced pore volume. This phenomenon has been previously observed and reported in several other studies in the literature [42–44]. As the pore volume increases, the BET surface area decreases due to the deposition of Pt and Co particles inside the pores.

### X-ray diffractometry (XRD) and X-ray photoelectron spectroscopy (XPS)

XRD diffraction patterns of the reduced catalysts, shown in Fig. 1(a), were obtained to confirm the crystal structure. A amorphous halo around $2\theta = 23°$ was observed for all the samples, which was assigned to SiO₂ (JCPDS No. 29–0085). The Pt/SiO₂ catalyst peaks were detected at $2\theta = 39.8°, 46.2°, 67.6°$, and $81.5°$, corresponding to the (111), (200), (220), (311) for Pt (JCPDS No. 01–1311) metal planes of the face-centered cubic



Fig. 1 — (a) X-ray diffractograms of the catalysts; XPS spectra of the Pt 4f region for the (b) Pt/SiO₂ and (c) PtCo/SiO₂ catalysts.

**Table 1 — Physical and chemical properties of the Pt/SiO₂, PtCo/SiO₂, and Co/SiO₂ catalysts.**

| Sample | Metal Loading (wt.%) | | Molar Ratio of Pt/Co | BET Surface Area (m²/g) | Total Pore Volume (cm³/g) |
|---|---|---|---|---|---|
| | Pt | Co | | | |
| SiO₂ | – | – | – | 448 | 0.64 |
| Pt/SiO₂ | 4.43 | – | – | 303.3 | 1.11 |
| PtCo/SiO₂ | 1.88 | 2.12 | 1 : 3.5 | 294.0 | 1.11 |
| Co/SiO₂ | – | 4.92 | – | 234.9 | 1.02 |

structure of Pt (FCC) structure, respectively. Furthermore, the peaks of Co/SiO$_2$ (JCPDS #15−0806), detected at $2\theta = 42.4°$, $51.8°$ and $77.6°$, correspond to the (111), (200), and (222) planes of the FCC structure of metallic cobalt (Co). Because Co is easily oxidized, the presence of the oxide phase is due to the exposure of the Co/SiO$_2$ sample to air prior to diffractometry. Notably, the XRD peaks for PtCo/SiO$_2$ were shifted to $2\theta = 40.4$ °and $46.8°$, indicating the presence of an PtCo alloy phase in the bimetallic catalyst [45]. While PtCo$_3$ alloy peaks were not detected for the tetragonal phase crystalline, a partial Pt$_3$Co alloy can be formed by adding Co to the Pt lattice [46]. Moreover, compared with Pt/SiO$_2$, the reduction in the lattice parameter of PtCo/SiO$_2$, as shown in Table 2, further corroborates the formation of an alloy phase in the bimetallic catalyst [45,47]. In other words, although the average particle size of Pt in both catalysts is similar, PtCo/SiO$_2$ exhibits broader diffraction peaks, strongly indicating the formation of defects and strain in the crystal lattice due to the PtCo alloy. However, it should be noted that this may also indicate the possible existence of larger particles (>10 nm) in the Pt/SiO$_2$ catalyst that were not detected in the TEM images. XPS measurements were performed to analyze the surface composition and chemical states of the catalysts. It should be noted that during exposure to air, the top surface of the pre-reduced sample may undergo oxidation. Fig. 1 (b) and (c) show the XPS spectra of the Pt/SiO$_2$ and PtCo/SiO$_2$ catalysts, respectively. The spectrum of Pt $4f_{7/2}$ of Pt/SiO$_2$ was deconvoluted into 71.1, 72.1, and 72.5 eV, corresponding to Pt(0), P(+2), and Pt(+4), respectively [48]. The respective peaks in the spectrum of Pt $4f_{5/2}$ of Pt/SiO$_2$ were also assigned to 74.4, 75.5, and 75.9 eV. On the other hand, the Pt $4f_{7/2}$ spectrum for PtCo/SiO$_2$ shifted to a higher binding energy than that of Pt/SiO$_2$. Pt(0) $4f_{7/2}$ is shifted to 71.4 eV, Pt(+2) $4f_{7/2}$ to 72.5 eV, and Pt(+4) $4f_{7/2}$ to 72.9 eV. Similarly, the respective peaks for Pt $4f_{5/2}$ also shifted to 74.7, 75.8, and 76.2 eV. This shift is associated with the downshift of the d-band center indicating successful formation of PtCo nanoalloys [49,50], which change the electronic structure of the Pt 4f orbital as a strong charge-transfer interaction occurs [51].

### TEM results

The dispersion and particle sizes of Pt and Co in the PtCo/SiO$_2$,Pt/SiO$_2$ and Co/SiO$_2$ catalysts are shown in the TEM images in Fig. 2. The average particle size of both the PtCo/SiO$_2$ and Pt/SiO$_2$ catalysts was approximately 1.3 nm (Table 2), indicating that the dispersion of the catalyst particles was unaffected by the addition of the Co promoter. The inset in Fig. 2(b) shows a high-resolution TEM image of a singular particle with a fringe distance (*d*) of approximately 2.15 Å that

corresponds to the (111) interplanar spacing of the PtCo alloy [52,53]. Furthermore, the EDS mapping of the bimetallic catalyst particles (inset in Fig. 2(c)) indicates that the larger Co particles are partially masked by the Pt nanoparticles. Based on these observations, it can be concluded that binary Pt−Co and alloyed PtCo particles are both present in the as-prepared bimetallic PtCo/SiO$_2$ catalyst. The Co/SiO$_2$ catalyst displayed chunks of Co particles larger than 5 nm, as seen in Fig. 2(h). This can be attributed to the significant agglomeration of Co on the catalyst surface, which agrees with the BET surface analysis results indicating the highest decrease in surface area for the Co/SiO$_2$ catalyst.

### H$_2$-TPR results

Fig. 3 shows the H$_2$-TPR profiles of Pt/SiO$_2$, PtCo/SiO$_2$, and Co/SiO$_2$ catalysts. The Pt/SiO$_2$ catalyst showed a broad peak around 150−450 °C, indicating the reduction of PtO$_X$ species interacting with the SiO$_2$ support. Reduction occurs from the surface to the bulk of the catalyst, resulting in a broad peak. This could be attributed to the reduction of Pt$^{4+}$ or Pt$^{2+}$ to Pt$^0$ [54]. The precursor used was H$_2$PtCl$_6$ which was reduced at lower temperatures (137−217 °C [55]); hence, the species reduced here were those anchored to the support [56]. The TPR curve for the Co/SiO$_2$ sample showed two steps of reduction. The first step of reduction is possibly attributed to the reduction from Co$_3$O$_4$ to CoO and/or CoO to Co, which is then further completely reduced to Co in the second step [57−59]. For the PtCo/SiO$_2$ catalyst, peaks were detected at approximately 176 and 348 °C. The Co$_3$O$_4$ reduction peak shifted to a lower temperature than that of the monometallic Co. The addition of noble metals (*e.g.*, Pt) has been reported to decrease the Co oxide reduction temperature via autocatalytic reduction and/or alloying, which promotes the dissociation and activation of H$_2$, thus facilitating the reduction of Co oxides [60−65]. This may indicate the formation of the alloy phase, as the Co reduction peaks are dramatically shifted to lower temperatures by hydrogen spillover from the highly adjacent Pt nanoparticles in their metallic states [66,67].

### EXAFS

The electronic and structural environments of the PtCo/SiO$_2$ catalysts were examined using XAS. The oxidation state of Pt was obtained by a linear combination method based on the two standards of Pt foil and PtO$_2$ representing Pt$^0$ and Pt$^{+4}$, respectively. As shown in Fig. 4(a), Pt was fairly reduced, indicating an average oxidation state of Pt$^{+1.3}$, which is in good agreement with the XPS results. The catalyst was reduced *ex situ* prior to the experiment; however, it was exposed to air during the sample preparation process. Because of the presence of oxidized Pt particles on the catalyst surface and the small Pt particle size, these results reveal that not all Pt atoms were alloyed with Co.

The $k^2$-weighted EXAFS spectrum of the PtCo/SiO$_2$ catalyst and the corresponding Fourier transform (FT) magnitudes are shown in Fig. 4(b) and (c). The EXAFS spectra were fitted using three single scattering paths: Pt−O, Pt−Co, and Pt−Pt (Table 3). The fitting results showed Pt−Pt bond length of 2.70 Å with a coordination number (CN) of 3.7 and Pt−Co bond length of

### Table 2 − Calculated lattice parameters and sizes of the Pt/SiO$_2$, PtCo/SiO$_2$ and Co/SiO$_2$ catalysts.

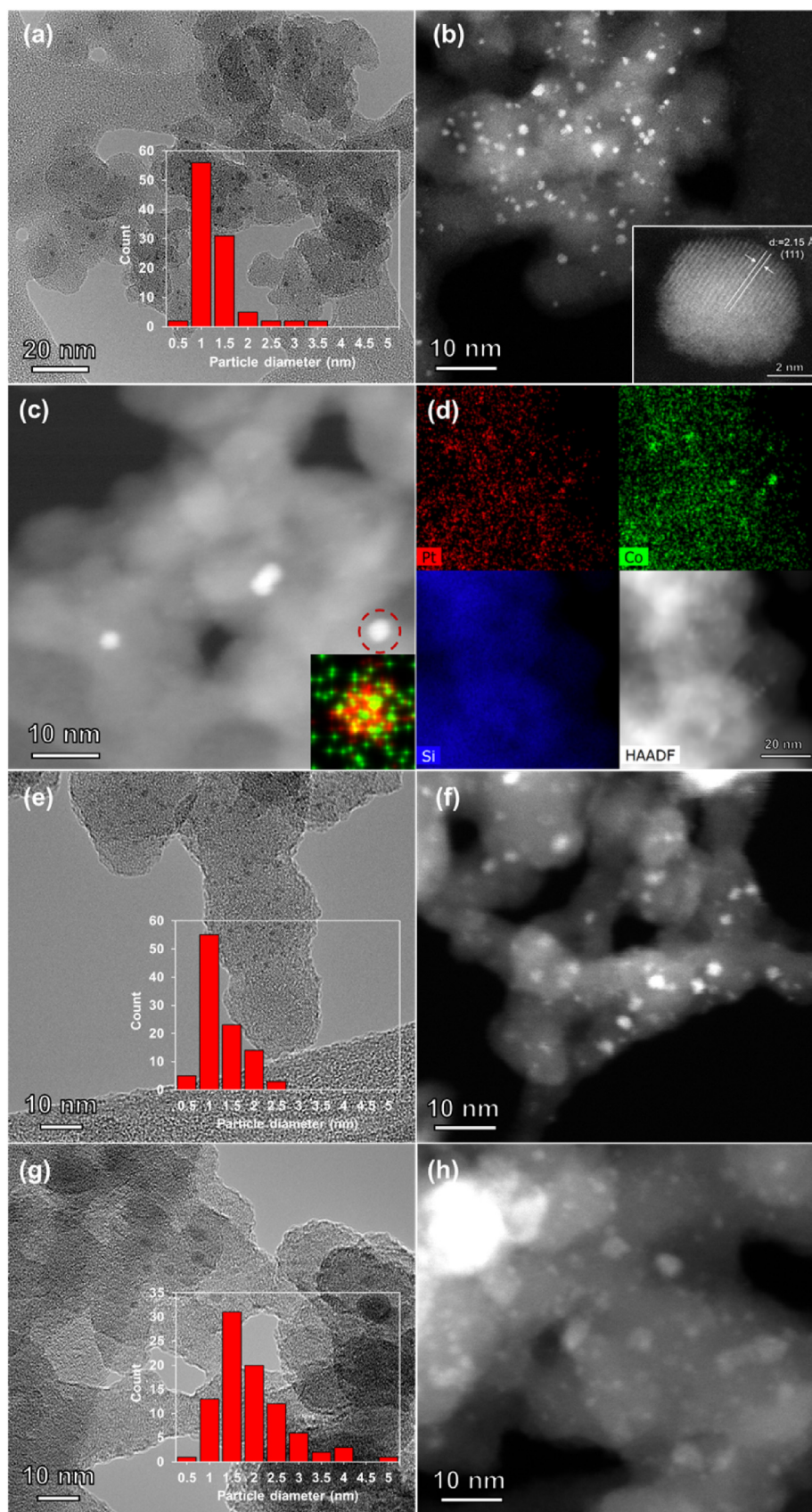| Sample | Lattice parameter (Å) - XRD | Averaged particle size (nm) - TEM |
|---|---|---|
| Pt/SiO$_2$ | 3.92 | 1.28 |
| PtCo/SiO$_2$ | 3.87 | 1.29 |
| Co/SiO$_2$ | 3.55 | 2.07 |

**Fig. 2** − **TEM images and particle-size histograms of (a−d) PtCo/SiO$_2$, (e, f) Pt/SiO$_2$, and (g, h) Co/SiO$_2$.**
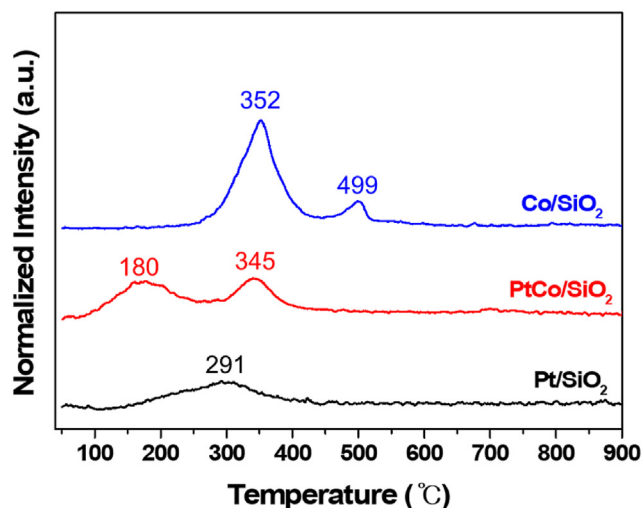
Fig. 3 — H$_2$-TPR profiles of the catalysts.

2.55 Å with a CN of 1.8. The calculated CN ratio of (Pt–Co)/(Pt–Pt) was 0.49, which corresponds to the Pt$_3$Co phase and is consistent with the values reported in the literature [68–70]. These results strongly suggest that the majority of Pt and Co exists as Pt$_3$Co nanoparticles on the SiO$_2$ support. Furthermore, Pt–O bond was confirmed with a bond length of 2.00 Å and a CN of 1.2. In line with the XANES results, oxidized Pt particles were observed on the surface. However, these particles are likely to be reduced to metallic Pt through in *situ* pre-reduction prior to the APR reaction.

### Activity results

*Optimization of the reaction conditions for high hydrogen production rate*
First, xylose reforming reaction conditions were optimized using a PtCo/SiO$_2$ catalyst to obtain the highest hydrogen production rate. As shown in Fig. 5(a), the WHSV values were varied at a reactor temperature of 225 °C and pressure of 29.3 bar. The catalytic activities are presented in Table 4. Both the H$_2$ production rate and H$_2$ selectivity increased with increasing WHSV from 2 to 8 h$^{-1}$. On the other hand, the conversion of C to gas (Table 4) was maximized at a WHSV of 2 h$^{-1}$ and decreased significantly at higher space velocities. In general, a higher C to gas conversion is achieved with decreasing WHSV values (greater amount of gas produced). It should be noted that during the experiment, the only carbon-containing gas detected was CO$_2$, and no CO or CH$_4$ was produced.

By increasing the WHSV from 8 h$^{-1}$ to 32 h$^{-1}$, both the H$_2$ production rate and the conversion of C to gas decreased rapidly. The H$_2$ selectivity dropped to 20%, and the H$_2$ production rate decreased to 3.4 μmol/min, implying a *ca.* 60% reduction compared with 8 h$^{-1}$. These results indicated that H$_2$ production was optimal when the space velocity was 8 h$^{-1}$. Although there was a steady decrease in the C-to-gas conversion from 2 h$^{-1}$ to 32 h$^{-1}$, the H$_2$ selectivity revealed a volcano plot.

Overall, increasing WHSV values indicate an injection of a larger amount of xylose, or in other words, carbon per unit
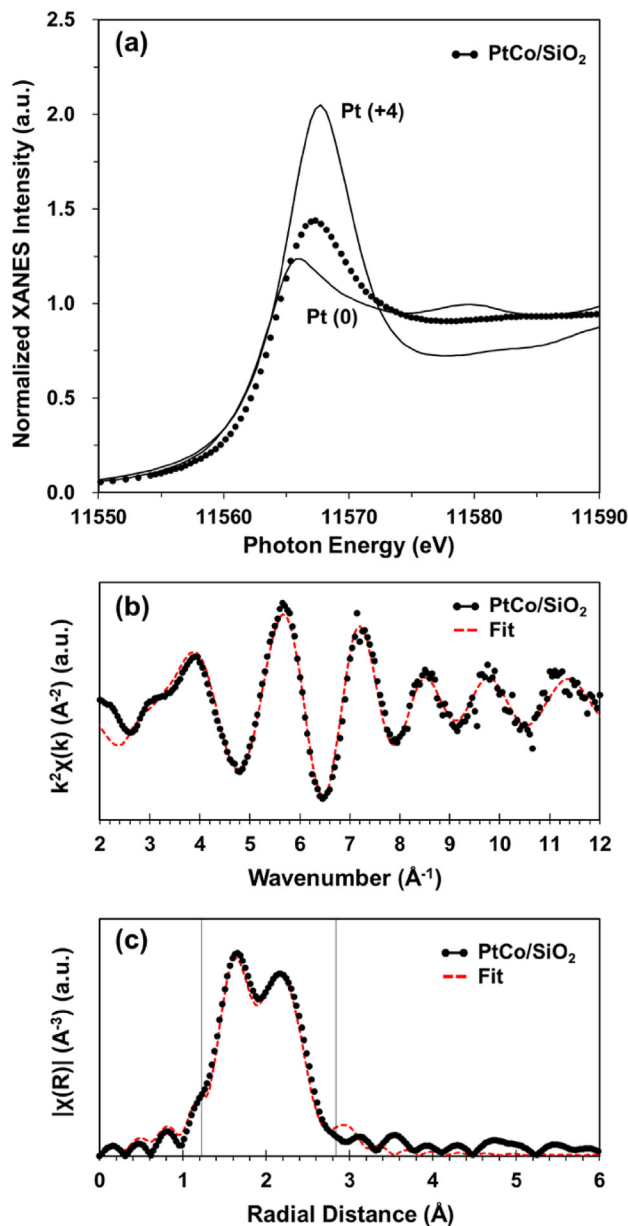


Fig. 4 — XANES and EXAFS spectra of PtCo/SiO$_2$.

Table 3 — EXAFS fitting results for PtCo/SiO$_2$. Pt L3 edge spectra were measured at RT; N, coordination number; ss, Debye–Waller factor; R, bond distance. Fitted range: $2.3 < k < 12.0$ Å$^{-1}$ and $1.2 < R < 2.8$ Å (k2 weighting).

| Samples | Scatter | N | ss (A$^2$) | R(Å) |
|---|---|---|---|---|
| Ru/H–Y | Pt–O | 1.2 (1) | 0.002 | 2.00 (1) |
| | Pt–Pt | 3.7 (2) | 0.013 | 2.70 (1) |
| | Pt–Co | 1.8 (2) | 0.007 | 2.55 (2) |

time over the same amount of catalyst into the reactor. Notably, the hydrogen selectivity is increased or maintained fairly constant with decreasing C to gas conversion WHSV from 2 to 8 h$^{-1}$, possibly implies that catalyst deactivation is not severe under these conditions and most carbon species dissolve in the liquid phase as by-products and/or long-chain
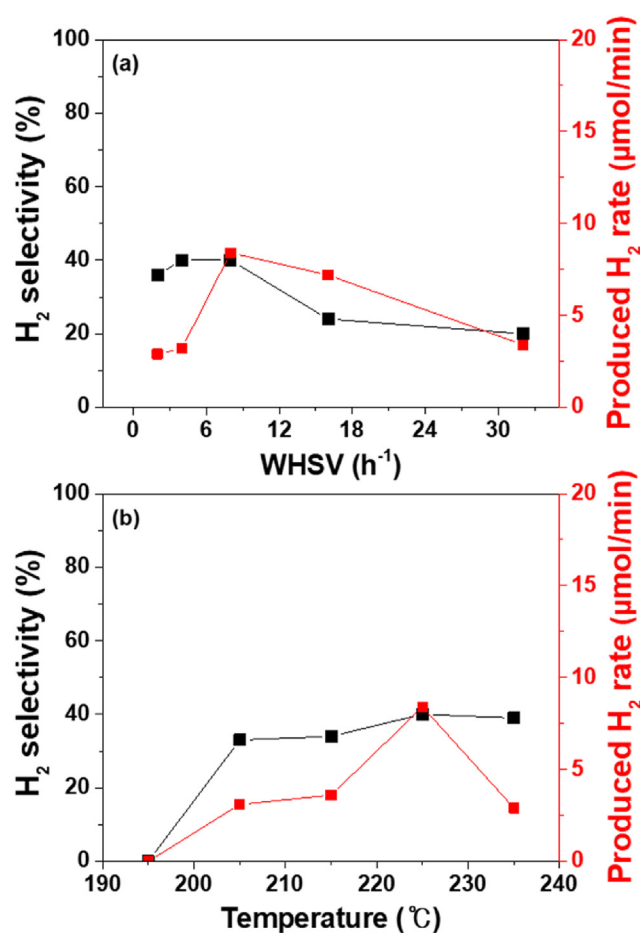
**Fig. 5 — Change in $H_2$ selectivity and $H_2$ production rate at different (a) WHSVs (T = 225 °C, P = 29.3 bar) and (b) temperatures (WHSV = 8 h$^{-1}$, P = 29.3 bar) using PtCo/SiO$_2$ catalyst.**

**Table 4 — Catalytic activity of PtCo/SiO$_2$ catalysts at different WHSVs (T = 225 °C, P = 29.3 bar) and temperatures (WHSV = 8 h$^{-1}$, P = 29.3 bar).**

| WHSV (h$^{-1}$) | 2 | 4 | 8 | 16 | 32 |
|---|---|---|---|---|---|
| $H_2$ selectivity (%) | 36 | 40 | **42** | 24 | 20 |
| $H_2$ production rate (µmol/min) | 2.9 | 3.2 | **8.4** | 7.2 | 3.4 |
| Conversion of C to gas (%) | 38 | 19 | **20** | 17 | 10 |
| Temperature (°C) | 205 | 215 | **225** | 235 | |
| $H_2$ selectivity (%) | 33 | 34 | **42** | 40 | |
| $H_2$ production rate (µmol/min) | 3.1 | 3.6 | **8.4** | 2.9 | |
| Conversion of C to gas (%) | 11 | 12 | **20** | 8 | |

carbon liquids. However, at higher WHSV values, catalyst deactivation becomes more pronounced due to the availability of more xylose, leading to severe coking, which subsequently results in decreased $H_2$ selectivity and C to gas conversion. This finding demonstrates the promising catalytic activity of PtCo/SiO$_2$ up to a WHSV value of 8 h$^{-1}$ resulting in a volcano plot in $H_2$ production rate.

Second, the effect of reaction temperature on the catalytic activity of PtCo/SiO$_2$ was investigated. The APR experiments were carried out by fixing the pressure at 29.3 bar and WHSV at 8 h$^{-1}$ while increasing the reaction temperature from 195 to

235 °C. It was found that the $H_2$ selectivity gradually increased and remained constant after 225 °C with 42% selectivity (Fig. 5(b), Table 4). The largest amount of $H_2$ was produced at 225 °C by 8.4 µmol/min, where the conversion of C to gas was optimized. However, at 235 °C, even though the $H_2$ selectivity was not significantly reduced (40%), a sudden drop in the $H_2$ production rate was observed (2.9 µmol/min).

The overall xylose reforming reaction is endothermic, which leads to increased catalyst activity with rising temperature. Thus, both the $H_2$ production rate and conversion of C to gas increase up to 225 °C, resulting an increase in $H_2$ selectivity. This reveals that 1) the catalyst is still active for APR of xylose up to 225 °C and 2) as the catalyst becomes more active, higher extent of carbon deposition on the catalyst surface and/or formation of by-product carbon species in the liquid phase occurs, reducing $CO_2$ formation in the gas phase and increasing hydrogen content in the product stream. However, at 235 °C, the catalyst significantly deactivates due to severe coking on its surface and possibly because of the formation of long-chain carbon liquids (alkanes) at higher reaction temperatures [71,72], which in turn decreased both the amount of $CO_2$ and $H_2$ produced. For example, similar trends in $H_2$ selectivity were observed in a study conducted by Wu et al. [73] on the APR of biodiesel byproduct glycerol, where the $H_2$ composition increased up to 225 °C from 180 °C and then suddenly dropped at 240 °C using Ni/CeO$_2$ and NiCu/CeO$_2$ catalysts.

*Xylose reforming reactivity of Pt/SiO$_2$, PtCo/SiO$_2$ and Co/SiO$_2$ catalysts*

The reforming activities of the Pt/SiO$_2$, PtCo/SiO$_2$, and Co/SiO$_2$ catalysts were examined while fixing the total metal loading of the catalyst to 5 wt % under optimized xylose APR conditions (225 °C, 29.3 bar, 8 h$^{-1}$). Pt has been reported to exhibit high selectivity for breaking C–C bonds, with high activity in $H_2$ production [24]. However, when supported on SiO$_2$, the hydrogen selectivity decreased from 43 to 17% as the reaction progressed for 3 h over the Pt/SiO$_2$ catalyst (Fig. 6(a)). The average $H_2$ production rate was 4.5 µmol/min (Table 5). In comparison, a significantly higher and stable $H_2$ selectivity of 42% with an averaged $H_2$ production rate of 8.4 µmol/min were obtained using PtCo/SiO$_2$ catalyst. It should be noted that Pt shows a C–C cleavage selectivity similar to that of bimetallic PtCo; however, Pt itself fails to maintain its activity owing to the strong adsorption of CO on the metal surface that was generated during the reaction. On the other hand, Co metal effectively reforms CO by increasing the water dissociation rate [74,75]. This facilitated the WGS reaction on the metal surface, significantly increasing catalytic activity. Hence, the amount of Pt loading was reduced by half, and the activity was improved by adding Co, compared to the monometallic Pt catalyst. Furthermore, the activity of Co in producing oxygen vacancies and promoting the reaction of oxygen and hydroxyl (OH) species from the dissociation of steam/water with oxygenate groups on the Co and/or Co-support interface reduces the formation of coke (coking) on the catalyst surface [35,76]. However, the catalytic activity results acquired over Co/SiO$_2$ indicated that a small amount of $CO_2$ was generated while the $H_2$ selectivity was at 0%, revealing that monometallic Co alone was inactive in the APR of xylose.
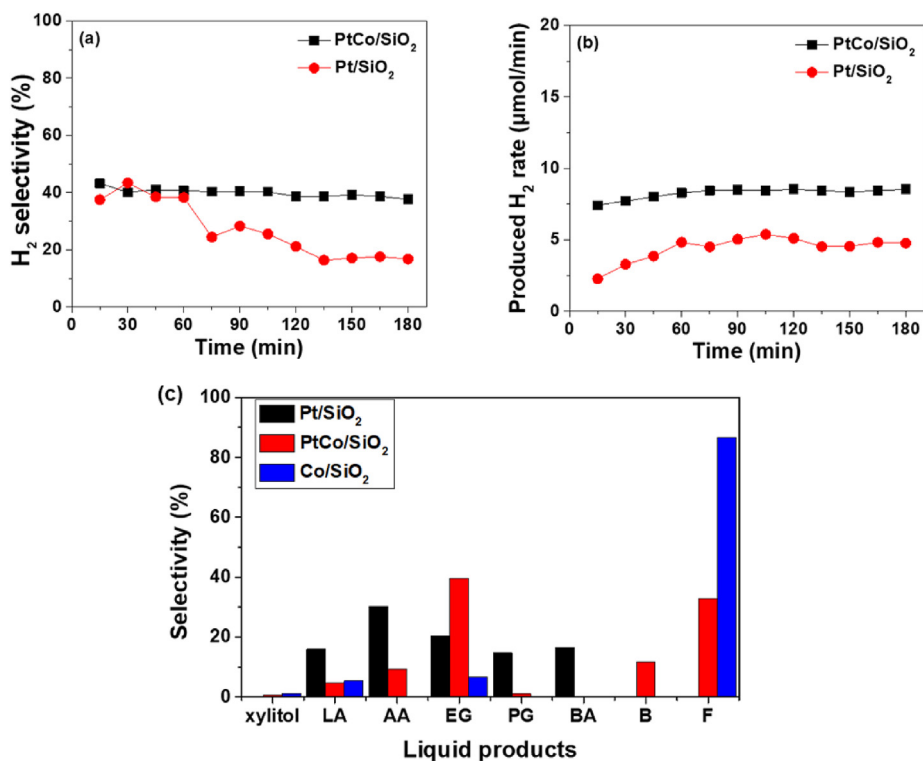
Fig. 6 — (a) $H_2$ selectivity and (b) $H_2$ production rate for PtCo/SiO$_2$ and Pt/SiO$_2$ catalysts, and (c) liquid product selectivity of different catalysts (T = 225 °C, P = 29.3 bar, WHSV = 8 h$^{-1}$).

Table 5 — Catalytic activities of Pt/SiO$_2$, PtCo/SiO$_2$ and Co/SiO$_2$ for the APR of xylose (T = 225 °C, P = 29.3 bar, WHSV = 8 h$^{-1}$).

|  |  | Catalyst | | |
| --- | --- | --- | --- | --- |
|  |  | PtCo/SiO$_2$ | Pt/SiO$_2$ | Co/SiO$_2$ |
| $H_2$ selectivity (%) |  | 42 | 17 | — |
| $H_2$ Production rate (μmol/min) |  | 8.4 | 4.5 | — |
| Conversion of C to gas (%) |  | 20 | 33 | 3.7 |
| Selectivity (%) of liquid byproducts | xylitol | 0.7 | — | 1.3 |
|  | lactic acid (LA) | 4.7 | 16 | 5.4 |
|  | acetic acid (AA) | 9.4 | 30.2 | — |
|  | ethylene glycol (EG) | 39.6 | 20.5 | 6.7 |
|  | 1,2-propanediol (propylene glycol, PG) | 1.1 | 14.8 | — |
|  | butyric acid (BA) | — | 16.6 | — |
|  | propanol | — | — | — |
|  | 2-butanol (B) | 11.7 | — | — |
|  | furfural (F) | 32.8 | — | 86.6 |
| Liquid byproducts (mmol/L) |  | 40.6 | 15.9 | 81.2 |
| Xylose conversion (%) |  | 100 | 99.9 | 99.6 |

Several intermediate liquid products are produced during the APR reaction, as shown in Fig. 6(c) and Table 5. In all cases, xylose was completely converted, with >99% xylose conversion, while organic acids and furfural were detected in all the catalyst formulations studied. These intermediates are produced via hydrogenation/hydrogenolysis and/or dehydration. In addition, it must be noted that long-chain carbon species derived from the polymerization and condensation of intermediate products that are not detectable by HPLC were present in the liquid phase. Fig. 7 shows the routes for xylose conversion in the APR. Based on the activity results, Co/SiO$_2$ favored the dehydration reaction by

C—O bond cleavage, resulting in the formation of large amounts of furfural (86.6%) [77]. In contrast, both the PtCo/SiO$_2$ and Pt/SiO$_2$ catalysts produced large amounts of ethylene glycol (EG) and 1, 2-propanediol (propylene glycol, PG). These two byproducts were produced by cleaving the C—C bond of xylitol, indicating that Pt and PtCo selectively break the C—C bonds. EG was produced the most (39.6%) using the PtCo/SiO$_2$ catalyst, which is an essential intermediate product to further produce $H_2$ through EG reforming. In contrast, the Pt/SiO$_2$ catalyst produced intermediates such as butyric acid (BA) and more PG and acetic acid via successive dehydration/hydrogenation reactions [72,78].
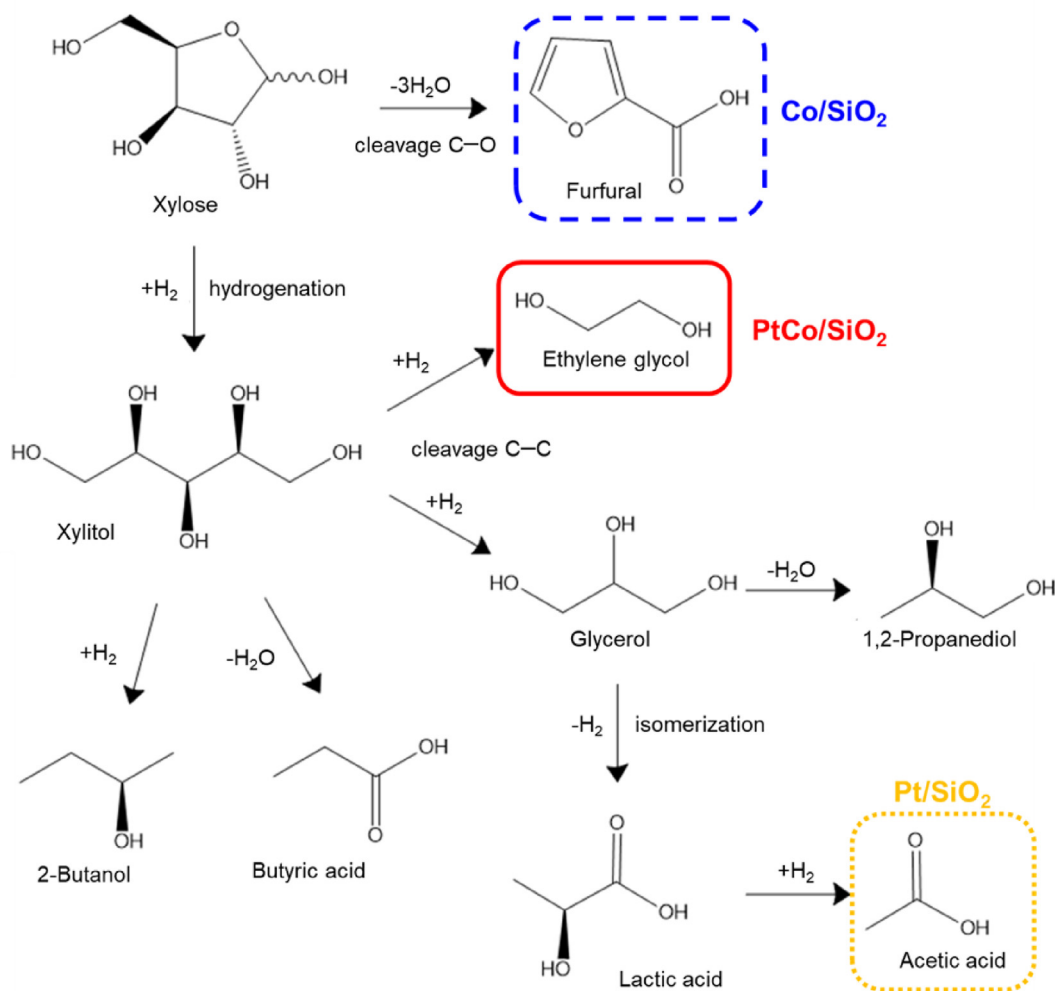
**Fig. 7 — Conversion routes of xylose in the APR.**

These results suggest that Pt/SiO$_2$ results in the consumption of H$_2$ by intermediate hydrogenation, contributing to a lower H$_2$ selectivity and production rate. Therefore, the presence of Co in the PtCo/SiO$_2$ catalyst shows a synergistic effect for the cleavage of the C–C bond, contributing to a higher H$_2$ selectivity than that of the monometallic Pt/SiO$_2$ catalyst.

## DFT calculation results

To estimate the reactivity of the total xylose dehydrogenation, the reaction energy ($\Delta E_r$) of the first dehydrogenation step from C$_5$H$_{10}$O$_5$ to C$_5$H$_9$O$_5$ [i.e., C$_5$H$_{10}$O$_5$* → C$_5$H$_9$O$_5$* + H*] was calculated. The adsorption and reaction energies were calculated using Eq. (5) and Eq. (6).
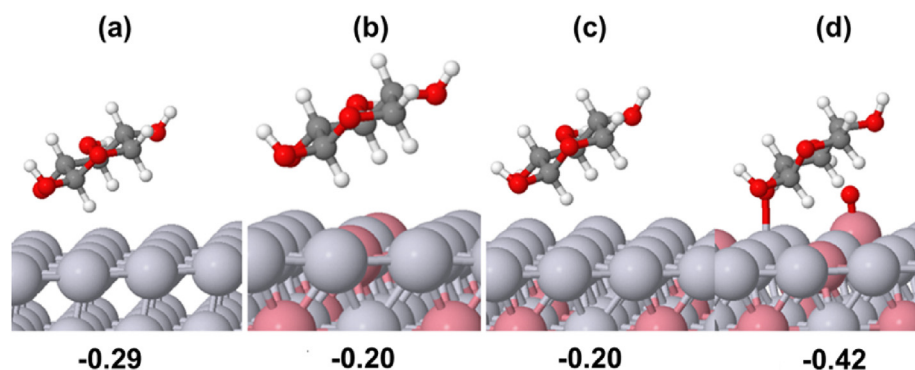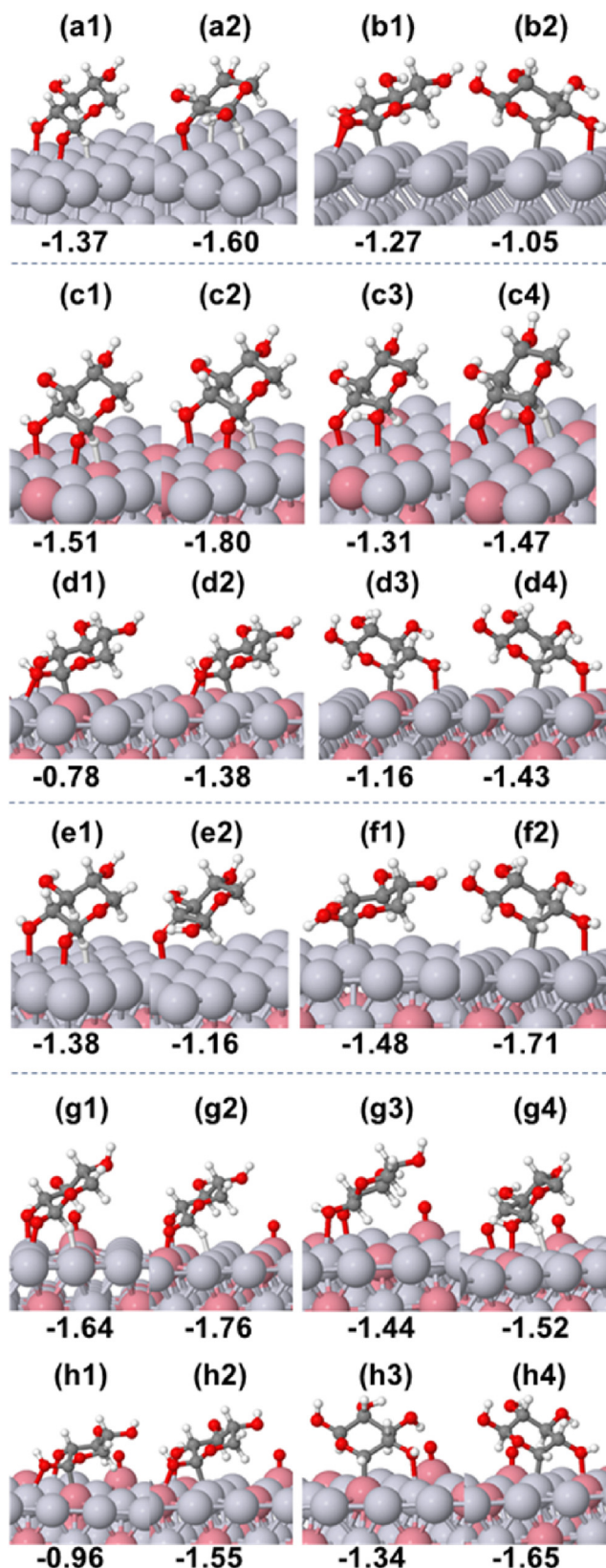


**Fig. 8 — Most optimized conformations of xylose on (a) Pt (111), (b) Pt$_3$Co (111), (c) Pt$_3$Co/Pt (111), and (d) Pt$_3$Co/O (111) surfaces. These values represent the adsorption energy in eV.**

**Fig. 9** — The most stable conformations of the xylose first dehydrogenation intermediate ($C_5H_9O_5$) on the Pt (111), $Pt_3Co$ (111), $Pt_3Co/Pt$ (111), and $Pt_3Co/O$ (111) surfaces. Conformations a, c, e, and g represent xylose dehydrogenation from the first and second O atom in the xylose's alcoholic group (counting in clockwise direction). In contrast, b, d, f, and h conformations represent xylose dehydrogenation from the first and second C atom separated by the xylose's alkoxy O atom. The values represent the adsorption energies in eV.

$$E_{ads} = E_{tot^*} - E_{slab} - E_{specie^*} \qquad (5)$$

$$\Delta E_r = \left(E_{C_5H_9O_5^*} + E_{H^*}\right) - \left(E_{C_5H_{10}O_5^*}\right) \qquad (6)$$

where $E_{ads}$ is the adsorption energy of any reaction species, including H atoms. $E_{slab}$ and $E_{tot}$ are the total energies of vacuum and adsorbate slabs, respectively. It is worth noting that various binding conformations of xylose and dehydrogenation intermediates were examined in this study, but the most optimal conformations are presented in Figs. 8 and 9, respectively.

According to Fig. 9, the strongest adsorbed xylose first-stage dehydrogenation intermediate ($C_5H_9O_5$) on Pt (111) and $Pt_3Co$ (111) was obtained from xylose dehydrogenation via the O atom. However, the same process occurs via the C atom of xylose on the $Pt_3Co/Pt$ (111) and $Pt_3Co/O$ (111) surfaces. Consequently, $C_5H_9O_5$ adsorption followed the order $Pt_3Co$ (111) > $Pt_3Co/O$ (111) > $Pt_3Co/Pt$ (111) > Pt (111). However, for the overall most stable conformations of xylose first dehydrogenated from either the O or C atom of xylose, the reaction energies shown in Table 6 follow the trend $Pt_3Co$ (111) < Pt (111) < $Pt_3Co/Pt$ (111) < $Pt_3Co/O$ (111).

Although the thermodynamics of the xylose first-stage dehydrogenation predicts an endothermic process on all the investigated surfaces, the $Pt_3Co$ (111) catalyst yielded the lowest reaction energy (see Table 6), along with a stronger affinity for $C_5H_9O_5$ (see Fig. 9). This result suggests that the incorporation of Co on the Pt (111) surface enhances xylose dehydrogenation. In the case of $Pt_3Co/Pt$ (111), a slightly lower affinity of $C_5H_9O_5$ than that of the $Pt_3Co$ (111) surface was observed, but a slightly stronger affinity compared to that of the Pt (111) surface. Nonetheless, thermodynamics (see Table 6) showed reduced activity compared to both Pt (111) and $Pt_3Co$ (111) surfaces. Similarly, $Pt_3Co/O$ (111) had a slightly weaker affinity for $C_5H_9O_5$ than the $Pt_3Co$ (111) surface but a slightly stronger affinity than both Pt (111) and $Pt_3Co/Pt$ (111) surfaces. However, thermodynamic analysis showed a dramatically reduced activity compared with the rest of the surfaces, implying that the presence of an oxidized Co atom on the $Pt_3Co$ (111) surface greatly hinders xylose dehydrogenation. In addition, to better understand the $Pt_3Co$ (111) catalyst's enhanced activity in line with its stronger affinity for $C_5H_9O_5$ compared to Pt (111), a density of state (DOS) electronic structure analysis was performed, as shown in Fig. 10. It is well known that, according to d-band theory, the up-shift of d-band center toward the Fermi level tends to increase binding strength between adsorbate and transition metal surface and vice versa [79]. In this case, it can be seen that on $Pt_3Co$ (111) there is an up-shift of the DOS for the surface Co atom compared to the surface Pt atom, leading to Co higher d-band center; $[\varepsilon_d$ (Co) = -1.27 eV] vs. $[\varepsilon_d$ (Pt) = -1.90 eV]. Moreover, when compared with the case of Pt (111), an up-shift of DOS

**Table 6 – Xylose-first dehydrogenation reaction energies on investigated surfaces. $\Delta E_{r,o}$ and $\Delta E_{r,c}$ denote the reaction energies from the xylose first dehydrogenation via xylose's O and C atoms (obtained from their most stable conformations on individual surfaces), respectively.**

| Surfaces | $\Delta E_{r,\,o}$ | $\Delta E_{r,\,c}$ |
|---|---|---|
| Pt (111) | **0.62** | 0.68 |
| Pt$_3$Co (111) | **0.46** | 0.60 |
| Pt$_3$Co/Pt (111) | 1.34 | **0.79** |
| Pt$_3$Co/O (111) | 1.16 | **1.05** |
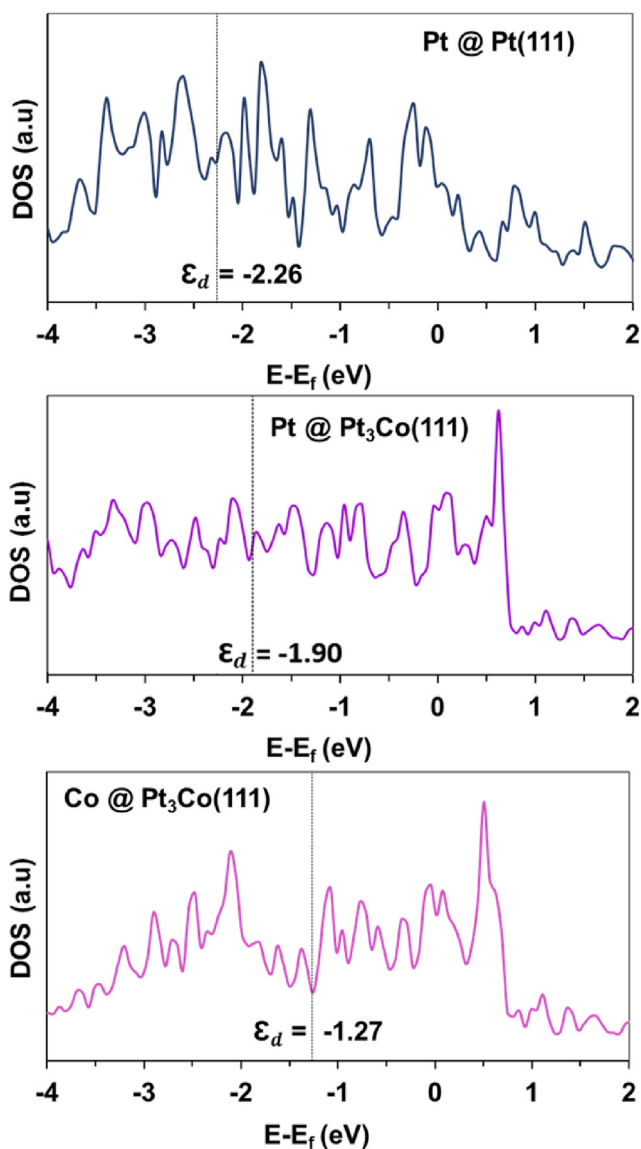


**Fig. 10 – Projected density of states (DOS) of surface atoms of Pt @Pt (111), Pt @ Pt$_3$Co (111), and Co @ Pt$_3$Co (111). The dotted lines denote the d-band centers ($\varepsilon_d$).**

for both Pt @ Pt$_3$Co (111) and Co @ Pt$_3$Co (111) compared to Pt @ Pt (111) [$\varepsilon_d$ (Pt) $= -2.26$ eV] was observed. This result suggests that the enhanced activity of Pt$_3$Co (111) is related to the surface layer of Co atoms.

The PtCo/SiO$_2$ catalyst employed in this study mainly consists of metallic Pt, Co, and Pt$_3$Co alloy sites during the APR of xylose. Evaluation of the catalytic activity data reveals that the metallic Co sites exhibit low activity levels when tested using a Co/SiO$_2$ catalyst, while the metallic Pt sites exhibit higher activity levels and are responsible for the C–C cleavage of the xylose-derived intermediates. The majority of the active sites in the PtCo/SiO$_2$ catalyst appear to be Pt$_3$Co alloy sites, as indicated by the observed changes in liquid product selectivity and increased catalytic activity compared to a Pt/SiO$_2$ catalyst. The Pt$_3$Co sites display a higher affinity towards the xylose first-stage dehydrogenation intermediate, as evidenced by DFT calculations, potentially enhancing C–C cleavage activity and leading to the formation of ethylene glycol while suppressing dehydration reactions that produce other liquid by-products.

## Conclusion

A bimetallic catalyst formulation (PtCo/SiO$_2$) was proposed and tested for the APR of xylose, which is an abundant and carbon-neutral H$_2$ source. Detailed morphological characterizations were performed to investigate the formation of bimetallic PtCo nanoparticles and/or nanoalloys. The APR conditions were optimized, and the catalytic activity and durability of the proposed bimetallic catalysts were experimentally investigated and benchmarked against their monometallic counterparts. Finally, the mechanism of the proposed catalyst is discussed. The following summarizes the principal findings of this study: TEM, XRD, XPS, and EXAFS results confirmed the partial formation of PtCo nanoalloy particles. PtCo/SiO$_2$ exhibited the highest H$_2$ selectivity (42%) and production rate (8.4 $\mu$mol/min). These are 2.47 and 1.87 times higher than Pt/SiO$_2$, respectively, whereas Co/SiO$_2$ exhibits no activity in H$_2$ production. Moreover, the selectivity of the PtCo/SiO$_2$ for liquid byproducts is 2.55 times higher than Pt/SiO$_2$, with ethylene glycol having the highest fraction (39.6%) among the liquid byproducts. Using PtCo/SiO$_2$, only 20% of the carbon was released as gas (CO$_2$) under the optimized reaction conditions, as opposed to 33% using Pt/SiO$_2$. In contrast, Co/SiO$_2$ produced a significant amount of furfural (86.6%). Therefore, not only does PtCo/SiO$_2$ have the highest activity, it also promotes the production of useful chemicals as byproducts. This is due to the high selectivity of the Co promoter in breaking C–C bonds (C–C cleavage). Finally, our proposed bimetallic catalyst offers a cost-effective, durable, and highly functional solution for carbon-neutral H$_2$ production and fuel production from hard-to-ferment xylose.

## Declaration of competing interest

The authors declare that they have no known competing financial interests or personal relationships that could have appeared to influence the work reported in this paper.

## REFERENCES

[1] Bauen A, Berndes G, Junginger HM, Londo M, Vuille F. Bioenergy - a sustainable and reliable energy source - a review of status and prospects. IEA Bioenergy ExCo 2009;vol. 6.

[2] Wang S, Dai G, Yang H, Luo Z. Lignocellulosic biomass pyrolysis mechanism: a state-of-the-art review. Prog Energy Combust Sci 2017;62:33—86.

[3] Lepage T, Kammoun M, Schmetz Q, Richel A. Biomass-to-hydrogen: a review of main routes production, processes evaluation and techno-economical assessment. Biomass Bioenergy 2021;144:105920.

[4] Hu X, Gholizadeh M. Biomass pyrolysis: a review of the process development and challenges from initial researches up to the commercialisation stage. J Energy Chem 2019;39:109—43.

[5] Heidenreich S, Foscolo PU. New concepts in biomass gasification. Prog Energy Combust Sci 2015;46:72—95.

[6] Adeniyi AG, Otoikhian KS, Ighalo JO. Steam reforming of biomass pyrolysis oil: a review. Int J Chem React Eng 2019;17.

[7] Østby H, Hansen LD, Horn SJ, Eijsink VGH, Várnai A. Enzymatic processing of lignocellulosic biomass: principles, recent advances and perspectives. J Ind Microbiol Biotechnol 2020;47:623—57.

[8] Levin DB, Pitt L, Love M. Biohydrogen production: prospects and limitations to practical application. Int J Hydrogen Energy 2004;29:173—85.

[9] Fasolini A, Cucciniello R, Paone E, Mauriello F, Tabanelli T. A short overview on the hydrogen production via aqueous phase reforming (APR) of cellulose. C6-C5 Sugars and Polyols, Catalysts 2019;9.

[10] Cortright RD. Hydrogen generation from biomass-derived compounds utilizing aqueous-phase reforming. 2005 IEEE Vehicle Power and Propulsion Conference 2005:3.

[11] Dahmen N, Dinjus E, Kruse A. Fuels — HYDROGEN PRODUCTION | biomass: thermochemical processes. In: Garche J, editor. Encyclopedia of electrochemical power sources. Amsterdam: Elsevier; 2009. p. 259—67.

[12] Lakhtaria P, Ribeirinha P, Huhtinen W, Viik S, Sousa J, Mendes A. Hydrogen production via aqueous-phase reforming for high-temperature proton exchange membrane fuel cells - a review [version 2; peer review: 1 approved]. Open Research Europe 2021;1.

[13] Pipitone G, Zoppi G, Frattini A, Bocchini S, Pirone R, Bensaid S. Aqueous phase reforming of sugar-based biorefinery streams: from the simplicity of model compounds to the complexity of real feeds. Catal Today 2020;345:267—79.

[14] Liu C-G, Xiao Y, Xia X-X, Zhao X-Q, Peng L, Srinophakun P, Bai F-W. Cellulosic ethanol production: progress, challenges and strategies for solutions. Biotechnol Adv 2019;37:491—504.

[15] Avanthi A, Kumar S, Sherpa KC, Banerjee R. Bioconversion of hemicelluloses of lignocellulosic biomass to ethanol: an attempt to utilize pentose sugars. Biofuels 2017;8:431—44.

[16] Zhao L, Chen C, Ren HY, Wang ZH, Wu KK, Meng J, Cao GL, Ren NQ, Ho SH. Unraveling hydrogen production potential by glucose and xylose co-fermentation of Thermoanaerobacterium thermosaccharolyticum W16 and

[17] its metabolisms through transcriptomic sequencing. Int J Energy Res 2020;44:9617—28.

[17] Zhao L, Guo W-Q, Guo X-C, Ren H-Y, Wu J-T, Cao G-L, Wang A-J, Ren N-Q. Continuous hydrogen production from glucose/xylose by an anaerobic sequential batch reactor to maximize the energy recovery efficiency. RSC Adv 2018;8:20712—8.

[18] Qiu C, Yuan P, Sun L, Wang S, Lo S, Zhang D. Effect of fermentation temperature on hydrogen production from xylose and the succession of hydrogen-producing microflora. J Chem Tech Biotechnol 2017;92:1990—7.

[19] Moradian JM, Xu Z-A, Shi Y-T, Fang Z, Yong Y-C. Efficient biohydrogen and bioelectricity production from xylose by microbial fuel cell with newly isolated yeast of Cystobasidium slooffiae. Int J Energy Res 2020;44:325—33.

[20] Kim Y, Kim M, Jeong H, Kim Y, Choi SH, Ham HC, Lee SW, Kim JY, Song KH, Yoon CW, Jo YS, Sohn H. High purity hydrogen production via aqueous phase reforming of xylose over small Pt nanoparticles on a γ-Al2O3 support. Int J Hydrogen Energy 2020;45:13848—61.

[21] Alcalá R, Mavrikakis M, Dumesic JA. DFT studies for cleavage of C-C and C-O bonds in surface species derived from ethanol on Pt(111). J Catal 2003;218:178—90.

[22] Ciftci A, Ligthart DAJM, Hensen EJM. Aqueous phase reforming of glycerol over Re-promoted Pt and Rh catalysts. Green Chem 2014;16:853—63.

[23] Huber GW, Shabaker JW, Dumesic JA. Raney Ni-Sn catalyst for $H_2$ production from biomass-derived hydrocarbons. Science 2003;300:2075—7.

[24] Pipitone G, Zoppi G, Pirone R, Bensaid S. A critical review on catalyst design for aqueous phase reforming. Int J Hydrogen Energy 2022;47:151—80.

[25] Davda RR, Alcalá R, Shabaker J, Huber G, Cortright RD, Mavrikakis M, Dumesic JA. 11 DFT and experimental studies of C-C and C-O bond cleavage in ethanol and ethylene glycol on Pt catalysts. In: Anpo M, Onaka M, Yamashita H, editors. Studies in surface science and catalysis. Elsevier; 2003. p. 79—84.

[26] Liu B, Greeley J. A density functional theory analysis of trends in glycerol decomposition on close-packed transition metal surfaces. Phys Chem Chem Phys 2013;15:6475—85.

[27] Davda RR, Shabaker JW, Huber GW, Cortright RD, Dumesic JA. Aqueous-phase reforming of ethylene glycol on silica-supported metal catalysts. Appl Catal B Environ 2003;43:13—26.

[28] Xi J, Xia Q, Shao Y, Ding D, Yang P, Liu X, Lu G, Wang Y. Production of hexane from sorbitol in aqueous medium over Pt/NbOPO4 catalyst. Appl Catal B Environ 2016;181:699—706.

[29] Sádaba I, López Granados M, Riisager A, Taarning E. Deactivation of solid catalysts in liquid media: the case of leaching of active sites in biomass conversion reactions. Green Chem 2015;17:4133—45.

[30] Rahman MM, Church TL, Variava MF, Harris AT, Minett AI. Bimetallic Pt—Ni composites on ceria-doped alumina supports as catalysts in the aqueous-phase reforming of glycerol. RSC Adv 2014;4:18951—60.

[31] El Doukkali M, Iriondo A, Cambra JF, Gandarias I, Jalowiecki-Duhamel L, Dumeignil F, Arias PL. Deactivation study of the Pt and/or Ni-based γ-Al2O3 catalysts used in the aqueous phase reforming of glycerol for H2 production. Appl Catal Gen 2014;472:80—91.

[32] Dal Santo V, Gallo A, Naldoni A, Guidotti M, Psaro R. Bimetallic heterogeneous catalysts for hydrogen production. Catal Today 2012;197:190—205.

[33] Dosso LA, Vera CR, Grau JM. Aqueous phase reforming of polyols from glucose degradation by reaction over Pt/alumina catalysts modified by Ni or Co. Int J Hydrogen Energy 2017;42:18853—64.

[34] Dietrich PJ, Sollberger FG, Akatay MC, Stach EA, Delgass WN, Miller JT, Ribeiro FH. Structural and catalytic differences in the effect of Co and Mo as promoters for Pt-based aqueous phase reforming catalysts. Appl Catal B Environ 2014;156–157:236–48.

[35] Gao X, Wang Z, Ashok J, Kawi S. A comprehensive review of anti-coking, anti-poisoning and anti-sintering catalysts for biomass tar reforming reaction. Chem Eng Sci X 2020;7:100065.

[36] Ravenelle RM, Copeland JR, Kim W-G, Crittenden JC, Sievers C. Structural changes of γ-Al2O3-supported catalysts in hot liquid water. ACS Catal 2011;1:552–61.

[37] Ravenelle RM, Copeland JR, Van Pelt AH, Crittenden JC, Sievers C. Stability of Pt/γ-Al2O3 catalysts in model biomass solutions. Top Catal 2012;55:162–74.

[38] United States Geological Survey, Mineral Commodity Summaries. Nitrogen (Fixed)—ammonia. January 2021. Retrieved from, https://pubs.usgs.gov/periodicals/mcs2021/mcs2021-nitrogen.pdf.

[39] Blöchl PE. Projector augmented-wave method. Phys Rev B 1994;50:17953–79.

[40] Perdew JP, Burke K, Ernzerhof M. Generalized gradient approximation made simple. Phys Rev Lett 1996;77:3865–8.

[41] Akpe SG, Choi SH, Ham HC. Conversion of cyclic xylose into xylitol on Ru, Pt, Pd, Ni, and Rh catalysts: a density functional theory study. Phys Chem Chem Phys 2021;23:26195–208.

[42] Yi M, Cheng Y, Wang C, Wang Z, Hu B, He X. Effects of composition changes of coal treated with hydrochloric acid on pore structure and fractal characteristics. Fuel 2021;294.

[43] Kruk M, Hui CM. Synthesis and characterization of large-pore FDU-12 silica. Microporous Mesoporous Mater 2008;114:64–73.

[44] Zhang A-B, Pan L, Zhang H-Y, Liu S-T, Ye Y, Xia M-S, Chen X-G. Effects of acid treatment on the physico-chemical and pore characteristics of halloysite. Colloids Surf A Physicochem Eng Asp 2012;396:182–8.

[45] Saejeng Y, Tantavichet N. Preparation of Pt–Co alloy catalysts by electrodeposition for oxygen reduction in PEMFC. J Appl Electrochem 2009;39:123–34.

[46] Dai S, You Y, Zhang S, Cai W, Xu M, Xie L, Wu R, Graham GW, Pan X. In situ atomic-scale observation of oxygen-driven core-shell formation in Pt3Co nanoparticles. Nat Commun 2017;8:204.

[47] Lopes T, Antolini E, Colmati F, Gonzalez ER. Carbon supported Pt–Co (3:1) alloy as improved cathode electrocatalyst for direct ethanol fuel cells. J Power Sources 2007;164:111–4.

[48] Vinayan BP, Ramaprabhu S. Platinum–TM (TM = Fe, Co) alloy nanoparticles dispersed nitrogen doped (reduced graphene oxide-multiwalled carbon nanotube) hybrid structure cathode electrocatalysts for high performance PEMFC applications. Nanoscale 2013;5:5109–18.

[49] Martinez G, Malumbres A, Lopez A, Mallada R, Hueso JL, Santamaria J. Laser-assisted production of carbon-encapsulated Pt-Co alloy nanoparticles for preferential oxidation of carbon monoxide. Front Chem 2018;6.

[50] Wakisaka M, Mitsui S, Hirose Y, Kawashima K, Uchida H, Watanabe M. Electronic structures of Pt–Co and Pt–Ru alloys for CO-tolerant anode catalysts in polymer electrolyte fuel cells studied by EC–XPS. J Phys Chem B 2006;110:23489–96.

[51] Zhang J-M, Sun S-N, Li Y, Zhang X-J, Zhang P-Y, Fan Y-J. A strategy in deep eutectic solvents for carbon nanotube-supported PtCo nanocatalysts with enhanced performance toward methanol electrooxidation. Int J Hydrogen Energy 2017;42:26744–51.

[52] Huang H, Hu X, Zhang J, Su N, Cheng J. Facile fabrication of platinum-cobalt alloy nanoparticles with enhanced electrocatalytic activity for a methanol oxidation reaction. Sci Rep 2017;7:45555.

[53] Ye X, Xue Y, Li K, Tang W, Han X, Zhang X, Song Z, Zheng Z, Kuang Q. Design of ternary Pt–CoZn alloy catalysts coated with N-doped carbon towards acidic oxygen reduction. Materials Advances 2021;2:5479–86.

[54] Almohalla M, Gallegos-Suarez E, Arcoya A, Rodríguez-Ramos I, Guerrero-Ruiz A. Comparative study of bioethanol transformation catalyzed by Ru or Pt nanoparticles supported on KL zeolite. Catal Sci Technol 2016;6:521–9.

[55] H. Knözinger, Temperature-Programmed Reduction and Oxidation 1 A list of symbols used in the text is provided at the end of the chapter, Handbook of Heterogeneous Catalysis, pp. 1080-1096.

[56] Barrales-Cortés CA, Pérez-Pastenes H, Piña-Victoria JC, Viveros-García T. Hydrogenation of citral on Pt/SiO2 catalysts: effect of Sn addition and type of solvent. Top Catal 2020;63:468–80.

[57] Teles CA, Rabelo-Neto RC, de Lima JR, Mattos LV, Resasco DE, Noronha FB. The effect of metal type on hydrodeoxygenation of phenol over silica supported catalysts. Catal Lett 2016;146:1848–57.

[58] Sun X, Suarez AIO, Meijerink M, van Deelen T, Ould-Chikh S, Zečević J, de Jong KP, Kapteijn F, Gascon J. Manufacture of highly loaded silica-supported cobalt Fischer–Tropsch catalysts from a metal organic framework. Nat Commun 2017;8:1680.

[59] Wu D, Jia R, Wen M, Zhong S, Wu Q, Fu Y, Yu S. Ultrastable PtCo/Co3O4–SiO2 nanocomposite with active lattice oxygen for superior catalytic activity toward CO oxidation. Inorg Chem 2020;59:1218–26.

[60] Diehl F, Khodakov AY. Promotion of cobalt fischer-tropsch catalysts with noble metals: a review, oil & gas science and Technology - rev. IFP 2009;64:11–24.

[61] Hilmen AM, Schanke D, Holmen A. TPR study of the mechanism of rhenium promotion of alumina-supported cobalt Fischer-Tropsch catalysts. Catal Lett 1996;38:143–7.

[62] Bruce LA, Hoang M, Hughes AE, Turney TW. Ruthenium promotion of fischer-tropsch synthesis over coprecipitated cobalt/ceria catalysts. Appl Catal Gen 1993;100:51–67.

[63] Jacobs G, Das TK, Zhang Y, Li J, Racoillet G, Davis BH. Fischer–Tropsch synthesis: support, loading, and promoter effects on the reducibility of cobalt catalysts. Appl Catal Gen 2002;233:263–81.

[64] Xiong M, Gao Z, Qin Y. Spillover in heterogeneous catalysis: new insights and opportunities. ACS Catal 2021;11:3159–72.

[65] Nabaho D, Niemantsverdriet JW, Claeys M, van Steen E. Hydrogen spillover in the Fischer–Tropsch synthesis: an analysis of platinum as a promoter for cobalt–alumina catalysts. Catal Today 2016;261:17–27.

[66] Guczi L, Bazin D, Kovács I, Borkó L, Schay Z, Lynch J, Parent P, Lafon C, Stefler G, Koppány Z, Sajó I. Structure of Pt–Co/Al2O3 and Pt–Co/NaY bimetallic catalysts: characterization by in situ EXAFS, TPR, XPS and by activity in Co (carbon monoxide) hydrogenation. Top Catal 2002;20:129–39.

[67] Jacobs G, Chaney JA, Patterson PM, Das TK, Maillot JC, Davis BH. Fischer-Tropsch synthesis: study of the promotion of Pt on the reduction property of Co/Al2O3 catalysts by in situ EXAFS of Co K and Pt LIII edges and XPS. J Synchrotron Radiat 2004;11:414–22.

[68] Cesar LG, Yang C, Lu Z, Ren Y, Zhang G, Miller JT. Identification of a Pt3Co surface intermetallic alloy in Pt–Co propane dehydrogenation catalysts. ACS Catal 2019;9:5231–44.

[69] Feiten FE, Takahashi S, Sekizawa O, Wakisaka Y, Sakata T, Todoroki N, Uruga T, Wadayama T, Iwasawa Y, Asakura K. Model building analysis — a novel method for statistical evaluation of Pt L3-edge EXAFS data to unravel the structure

of Pt-alloy nanoparticles for the oxygen reduction reaction on highly oriented pyrolytic graphite. Phys Chem Chem Phys 2020;22:18815–23.

[70] Lima FHB, Salgado JRC, Gonzalez ER, Ticianelli EA. Electrocatalytic properties of PtCo/C and PtNi/C alloys for the oxygen reduction reaction in alkaline solution. J Electrochem Soc 2007;154:A369.

[71] Chheda JN, Dumesic JA. An overview of dehydration, aldol-condensation and hydrogenation processes for production of liquid alkanes from biomass-derived carbohydrates. Catal Today 2007;123:59–70.

[72] Huber GW, Dumesic JA. An overview of aqueous-phase catalytic processes for production of hydrogen and alkanes in a biorefinery. Catal Today 2006;111:119–32.

[73] Wu K, Dou B, Zhang H, Liu D, Chen H, Xu Y. Aqueous phase reforming of biodiesel byproduct glycerol over mesoporous Ni-Cu/CeO2 for renewable hydrogen production. Fuel 2022:308.

[74] Mao J, He C-T, Pei J, Chen W, He D, He Y, Zhuang Z, Chen C, Peng Q, Wang D, Li Y. Accelerating water dissociation kinetics by isolating cobalt atoms into ruthenium lattice. Nat Commun 2018;9:4958.

[75] Gunasooriya GTKK, Saeys M. CO adsorption on Pt(111): from isolated molecules to ordered high-coverage structures. ACS Catal 2018;8:10225–33.

[76] Takise K, Higo T, Mukai D, Ogo S, Sugiura Y, Sekine Y. Highly active and stable Co/La0.7Sr0.3AlO3−δ catalyst for steam reforming of toluene. Catal Today 2016;265:111–7.

[77] Cao A, Schumann J, Wang T, Zhang L, Xiao J, Bothra P, Liu Y, Abild-Pedersen F, Nørskov JK. Mechanistic insights into the synthesis of higher alcohols from syngas on CuCo alloys. ACS Catal 2018;8:10148–55.

[78] Kirilin A, Wärnå J, Tokarev A, Murzin DY. Kinetic modeling of sorbitol aqueous-phase reforming over Pt/Al2O3. Ind Eng Chem Res 2014;53:4580–8.

[79] Hammer B, Nørskov JK. Theoretical surface science and catalysis—calculations and concepts, Advances in catalysis. Academic Press; 2000. p. 71–129.